IOP Publishing Mater. Quantum Technol. 5 (2025) 041001 https://doi.org/10.1088/2633-4356/ae1347

Materials for Quantum Technology

OPEN ACCESS

RECEIVED
29 May 2025

REVISED
15 September 2025

ACCEPTED FOR PUBLICATION
14 October 2025

PUBLISHED
23 October 2025

LETTER

The effect of niobium thin film structure on losses in superconducting circuits

Maxwell Drimmer[1,2,4,*], **Sjoerd Telkamp**[1,2,4], **Felix L Fischer**[1,2,4], **Ines C Rodrigues**[1,2], **Clemens Todt**[1,2], **Filip Krizek**[3], **Dominik Kriegner**[3], **Christoph Müller**[3], **Werner Wegscheider**[1,2] and **Yiwen Chu**[1,2]

[1] Department of Physics, ETH Zürich, 8093 Zürich, Switzerland
[2] Quantum Center, ETH Zürich, 8093 Zürich, Switzerland
[3] Institute of Physics, Czech Academy of Sciences, Cukrovarnická 10, 162 00 Praha 6, Czech Republic
[4] These authors contributed equally to the work.
[*] Author to whom any correspondence should be addressed.

E-mail: max.drimmer@phys.ethz.ch

Keywords: superconductors, sputtering, crystal structure, two level systems, quasiparticles, cryogenic microwave loss, superconducting circuits

Abstract

The performance of superconducting microwave circuits is strongly influenced by the material properties of the superconducting film and substrate. While progress has been made in understanding the importance of surface preparation and the effect of surface oxides, the complex effect of superconductor film structure on microwave losses is not yet fully understood. In this study, we investigate the microwave properties of niobium resonators with different crystalline properties and related surface topographies. We analyze a series of magnetron sputtered films in which the Nb crystal orientation and surface topography are changed by varying the substrate temperatures between room temperature and 975 K. The lowest-loss resonators that we measure have quality factors of over 10^6 at single-photon powers, among the best ever recorded using the Nb on sapphire platform. We observe the highest quality factors in films grown at an intermediate temperature regime of the growth series (550 K) where the films display both preferential ordering of the crystal domains and low surface roughness. Furthermore, we analyze the temperature-dependent behavior of our resonators to learn about how the quasiparticle density in the Nb film is affected by the niobium crystal structure and the presence of grain boundaries. Our results stress the connection between the crystal structure of superconducting films and the loss mechanisms suffered by the resonators and indicate that even a moderate change in temperature during thin film deposition can significantly affect the resulting quality factors.

The effort to build large-scale quantum processors has emphasized how studying materials can improve the lifetime and coherence of quantum systems [1–3]. Superconducting microwave resonators are often used to investigate loss in superconducting qubits because they are generally simpler to fabricate and measure while all sources of relaxation and decoherence affecting the performance of a resonator will also impact the performance of a qubit made from the same material [4]. Additionally, there are other applications that benefit from superconducting resonators with low levels of microwave dissipation, such as parametric amplifiers [5], quantum sensors [6], and microwave kinetic inductance detectors [7] used for astronomy and particle physics [8].

Measurements of superconducting resonators can distinguish between different sources of loss by determining the losses dependence on temperature and applied power. Dissipation at low microwave power and low temperature is especially relevant for quantum information processing [9]. In this regime, a common limiting loss mechanism is dielectric loss due to two-level systems (TLSs), and extensive work has been conducted in different material systems to locate and quantify this loss [10]. Oxides and impurities in close vicinity to the superconductor are a commonly observed cause of degradation of superconducting properties as they can host TLS [11, 12]. Many investigations attempting to

reduce TLS loss have focused on the removal of unwanted oxides and impurities from different interfaces through etching or cleaning steps. Pre-deposition cleaning steps of the substrate to avoid metal-substrate interface losses [13–18], as well as post-deposition processing steps of both substrate and deposited metal to reduce losses at the exposed surfaces [11, 12, 19–24] have been investigated intensively. However, the connection between the superconductor film structure, which is determined by the deposition process, and the microwave loss suffered by circuits is not as well understood. Differences in the deposition process have been previously studied by some authors [15, 25, 26] who also report changes in microwave properties, but an accurate description of the effect of film crystal properties on TLS loss as well as other loss mechanisms has not yet been established.

Our study focuses on niobium, commonly used in the superconducting circuits community [1], because it has the highest critical temperature and critical magnetic field of any elemental superconductor [27]. Furthermore, mono-crystalline Nb growth is possible at sufficiently high temperature and optimized growth conditions [25]. Sapphire substrates offer good thermal as well as chemical stability and have a small lattice mismatch with the Nb lattice, which allows for epitaxial growth [28]. This epitaxial match between the Nb film and substrate could allow for more mono-crystalline Nb films with minimal strain build-up at the interface. These key properties make Nb on sapphire suitable material platform to study the effect of crystallinity changes on superconducting resonator performance.

We present a study in which we systematically investigate the effect of the Nb crystal properties and interface epitaxy on the behavior and performance of superconducting microwave resonators. In the first part of this study, we investigate the influence of the Nb growth temperature on the film crystallinity as well as surface morphology and interface epitaxy towards the sapphire substrate. The observed crystal structure and morphology are then compared with DC superconducting transport characteristics. In the second part, we characterize coplanar waveguide (CPW) resonators and explore their low-temperature microwave properties. Specifically, we investigate the relationship between thin film crystallinity as well as general morphology and the single-photon quality factors that we measure. Furthermore, we study power-independent (PI) losses and relate them to the grain structure of the superconducting films.

1. Niobium thin film crystal properties

The crystal properties of a sputtered superconducting film can be affected by varying the substrate temperature during the deposition. If the substrate temperature is relatively low, deposited material forms a poly-crystalline film consisting of small crystal grains without a preferred orientation. At higher temperature, adatoms on the surface are supplied with increased energy that results in enhanced surface mobility. This leads to self-assembly into larger grains that are oriented in the most energetically favorable way, which in turn has an effect on the film morphology as described by a Thornton zone diagram [29–31]. Furthermore, substrate temperature can affect the degree to which the ion-to-atom ratio affects the morphology of the Nb film [32]. We studied five thin film depositions, listed in table 1, which were performed at various temperatures while all of the other deposition conditions were kept the same. A detailed growth procedure can be found in appendix A.

Figure 1(a) shows x-ray diffraction (XRD) traces of the Nb films. Various Nb diffraction lines are indicated in the figure. Film **A** that was deposited at room temperature shows signatures of all the commonly observed diffraction lines of poly-crystalline Nb, namely 110, 200, 211, and 220 [33]. See appendix B for additional details.

We observe a clear crossover in crystallinity from poly-crystalline at room temperature (Wafer **A**) to mono-crystalline at 975 K (Wafer **E**). The crystallographic changes become apparent at 550 K (Wafer **B**), where the [211] crystal orientation disappears and exclusively the [110] out-of-plane orientation is observed. At 745 K (Wafer **C**) the dominant out-of-plane crystal orientation changes to the [111] direction, which can be seen by the directly related 222 peak indicated in figure 1 that is not visible in Wafers **A** or **B**. Although the [111] out-of-plane crystal orientation appears to be dominant at 745 K and 900 K (Wafers **C** and **D**), other minor contributions such as the [110] orientation in **C** and the [200] orientation in **D** still remain. Finally, at 975 K the 222 peak is the only visible peak associated with Nb in the XRD spectrum which indicates that we have grown a mono-crystalline film with [111] out-of-plane orientation. We do not directly observe the 111 peak because it is a forbidden reflection for Nb.

This crystallographic crossover from poly-crystalline to mono-crystalline is confirmed by the XRD polefigures shown in figure 1(b). In this figure, a stereographic projection of the diffraction signal from the 110 lattice planes is shown, from which we can also asses the in-plane crystal orientations. The signal in the center of the figure corresponds to an out-of-plane [110] orientation. For film **A**, the figure shows an almost homogeneous distribution of diffraction intensity. This indicates that there is no directional preference of the crystal grains and is consistent with a poly-crystalline film. Starting at 550 K, dominant

Table 1. Overview of the sputtering conditions of the five wafers investigated in this study.

Wafer	A	B	C	D	E
Temperature (K)	300	550	745	900	975
Pressure (mBar$\times 10^{-3}$)	8.8	8.8	8.8	8.8	8.8
Power (W)	125	125	125	125	125

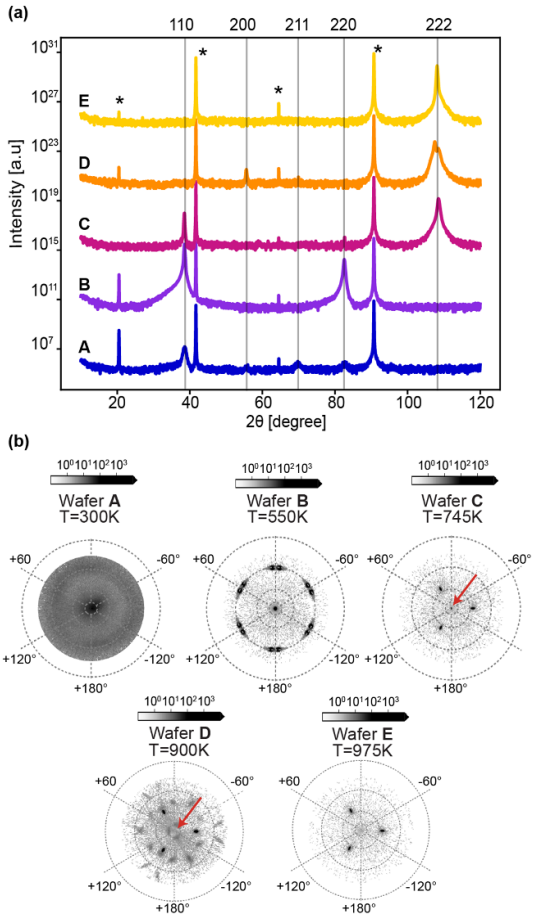

Figure 1. (a) XRD radial scans of the wafers listed in table 1. The traces are offset with respect to each other for clarity. The sharp peaks that are associated with the mono-crystalline sapphire substrate are labeled with a star. All observed Nb crystal orientations are indicated by vertical lines and labeled on top of the figure. XRD measurements were performed using monochromatic x-ray photons with $CuK_{\alpha 1}$ wavelength. (b) XRD polefigures of the 110 Bragg peak showing the orientation distribution of the [110] direction for films deposited at various temperatures.

crystal grain orientations are formed as indicated by discrete features in the polefigure. At 745 K, highly intense diffraction spots appear which are consistent with the [111] out-of-plane orientation. The three observed peaks correspond to the three-fold rotation axis around the [111] direction. A weak contribution in the center of the polefigure remains at 745 K, which is indicated by a red arrow. This central contribution then disappears at 900 K in Wafer **D**, indicating further alignment in the [111] out-of-plane crystal orientation. However, this crystallographic change is accompanied by some minor contributions at 900 K that are not aligned with the dominant orientation. We attribute this intermediate increase in crystal alignment disorder to increased strain associated with the process of alignment of all domains in the [111] crystal orientation. At 975 K, a completely mono-crystalline structure with [111] out-of-plane orientation is formed and no other orientations can be detected within the probed area of several mm^2.

The deposition temperature also influences the surface roughness of the sputtered Nb film. The surface topography was measured using atomic force microscopy (AFM) for each individual wafer directly after growth and is shown in figure 2(a). The surface of the wafer grown at room temperature clearly consists of small grains with no apparent preferential orientation. This grain structure of Nb has been frequently observed on a large variety of substrates such as Si [34] and GaAs [35]. A distinct triangular pattern appears at 550 K which becomes more evident at 700 K. This pattern, which is consistent

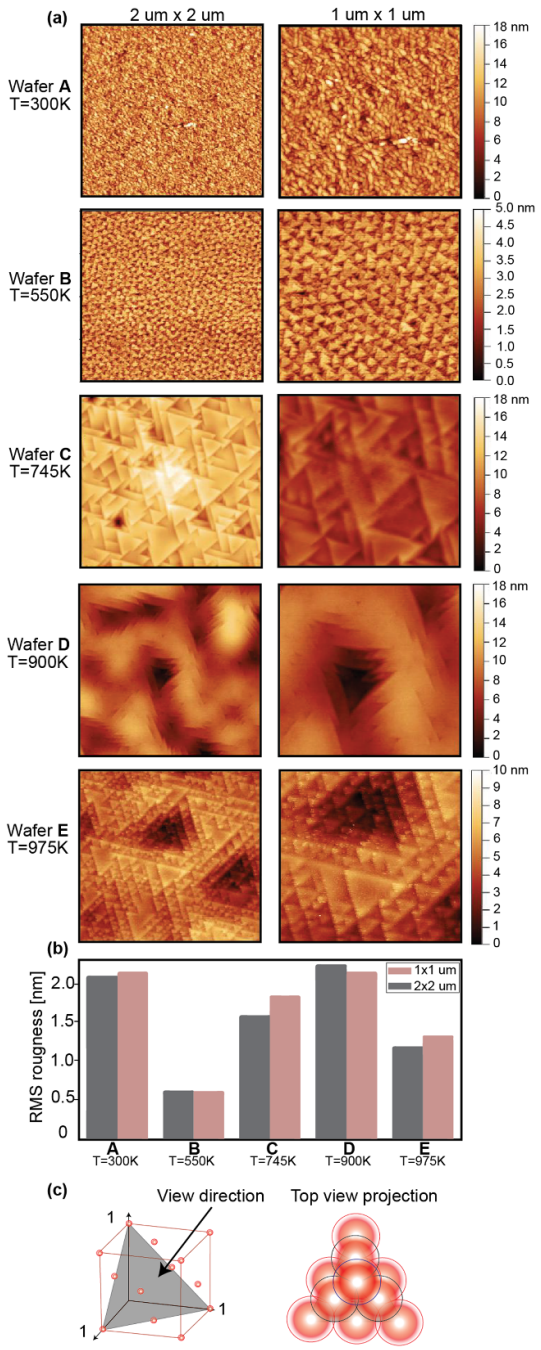

Figure 2. An overview of the effect of deposition temperature on Nb surface morphology studied by AFM topography images. In (a), Wafer **A** shows the commonly observed randomly oriented grain structure of Nb while the wafers grown at higher temperature start to display a triangular pattern that can be associated with the [111] direction viewed from the top (as indicated in (**c**)). Figure (b) shows the R_q surface roughness parameter associated with each wafer for both the $1 \times 1\ \mu$m as well as the $2 \times 2\ \mu$m surface area.

with the [111] orientation, remains visible at 900 K and 975 K but the size and exact shape of the features continues to change. The schematic in figure 2(c) illustrates how a top view of the Nb (111) lattice planes could result in the observed triangular geometry. Our data suggests that the crystal domains grow in size and consequently change the surface roughness and morphology in a complex process of self-assembly during growth. The effect on the root-mean-square (RMS) surface roughness calculated from the $2 \times 2\ \mu$m and $1 \times 1\ \mu$m AFM areas is plotted in figure 2(b). It is evident from this plot that Wafer **B** has the lowest surface roughness.

Another key feature that is known to have an effect on superconducting microwave resonator performance is the quality of the interface between the superconductor and the substrate [36]. We investigated the Al_2O_3–Nb interface of Wafers **A**, **B** and **D** using scanning transmission electron microscopy (STEM). In figure 3(a), it can be observed that for films grown at room temperature, a high-quality

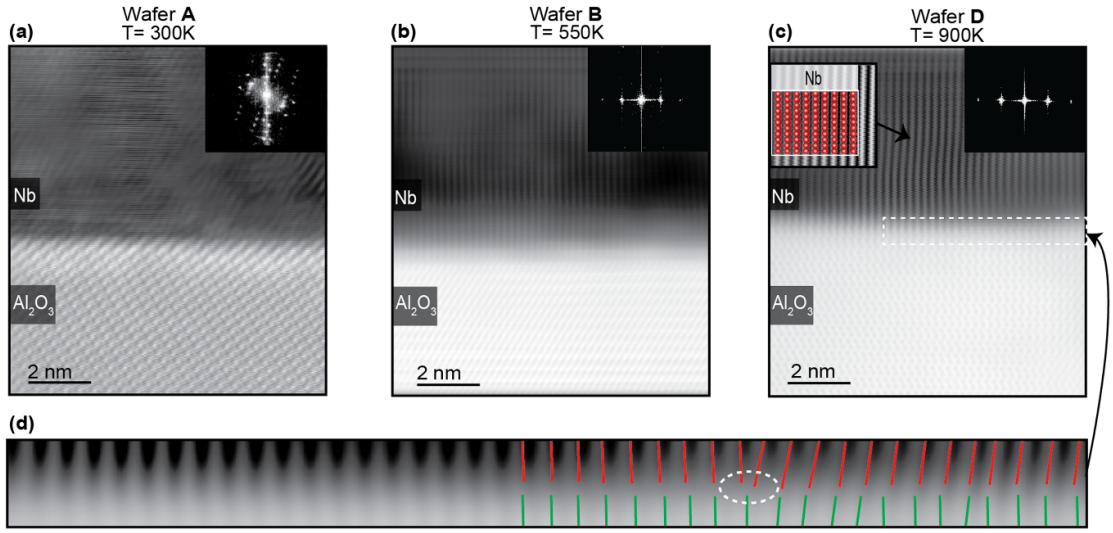

Figure 3. STEM images of Nb to sapphire interfaces of wafers grown at various temperatures. (a) A bright field STEM image in which a high-quality non-epitaxial interface is observed between the sapphire substrate and the poly-crystalline Nb film grown at room temperature (Wafer **A**). (b) A similar image of the interface between the Nb grown at 550 K and the sapphire substrate (Wafer **B**). In (c) the interface for Wafer **D** including a crystallographic model showing the Nb crystal lattice is shown. The zone axis differs between the images. In (d), a Bragg filtered image of a portion of the interface in (c) is shown in which the formation of sporadic misfit dislocations is indicated.

non-epitaxial interface is obtained that does not show any signs of oxides or chemical intermixing. The poly-crystalline character of the Nb layer is further substantiated by the ring-shaped pattern observed in the fast Fourier transform (FFT) image in the top right corner. At intermediate growth temperatures, it can be seen in figure 3(b) that an interface with a high degree of epitaxy between the sapphire (0001) and the Nb (110) crystals forms. Some variation in grain alignment was observed on the length scale of the lamella window ((1.5 μm) for Wafer **B**. In figure 3(c), the Nb to sapphire interface of Wafer **D** is shown. For this wafer, no grain boundaries were observed on the length scale of the lamella window and the Nb (111) to sapphire interface seems fully epitaxial. Therefore, we conclude that the (200) peak observed in the XRD measurements shown in figure 1 is only a very minor portion of the total crystal structure. A crystallographic model of the Nb lattice made using crystal visualization software (VESTA [37]) is overlaid with a zoomed-in part of the figure and shows agreement with the image. The intense highly symmetrical features of the FFT in the in-set of figure 3(c) clearly confirm the single crystalline nature and high degree of epitaxy in the measured portion of the film. The strain relaxation by the formation of a periodic array of misfit dislocation can be deduced from the Bragg filtered image of Wafer **D** shown in figure 3(c).

2. DC transport characterization

Before fabricating the resonators, the critical temperature and magnetic field of the superconducting Nb films were measured to benchmark the quality of the growth. Low-temperature DC transport measurements were performed in a Van der Pauw geometry using standard lock-in techniques to obtain the T_c and B_c of our wafers. All of the films have critical temperatures around 9.25 ± 0.1 K, which is close to the maximum bulk value of Niobium of 9.3 K [38]. We found that the critical magnetic field was consistently higher for the films with a lower degree of crystallinity. This can be attributed to superconducting vortices that are formed in the mixed state ($B > B_{c1}$) and are pinned on grain boundaries in the material [39]. More details on these measurements can be found in appendix C.

Table 2 contains metrics that we derive from these DC measurements. The mean free path l_{MFP} and the coherence length $\xi_{\mathrm{GL}}(0)$ are determined from these measurements since they can be used to identify possible sources of decoherence and they can be used to compare our thin film quality to other studies. We note that because the crystal structure changes from mono-to polycrystalline in this dataset, some assumptions about these metrics do not hold for some of our films. Despite this, we quote them here because we feel that they provide useful comparisons between our films. For details on the calculation and applicability of these length scales, see appendix C.

Table 2. The residual resistivity at 10 K ρ_{10K}, the mean free path length l_{MFP} (as defined in appendix C, see equation (C3)), and a coherence length metric $\xi_{GL}(0)$ determined from the critical magnetic field values shown in figure 7 using the Ginzburg–Landau relation applied at zero temperature.

Wafer	A	B	C	D	E
ρ_{10K} ($\mu\Omega$cm)	4	2.3	1.1	0.77	0.74
l_{MFP} (nm)	9	16	34	48	50
$\xi_{GL}(0)$ (nm)	14	20	23	23	23

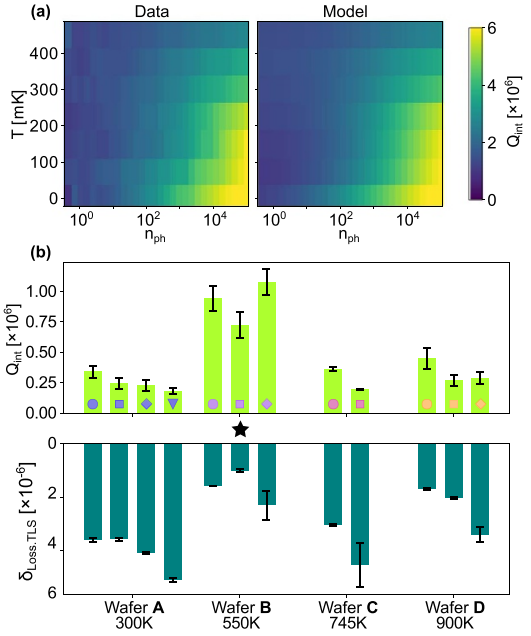

Figure 4. (a) Temperature and power dependence measured of the quality factor of the starred resonator from Wafer **B** marked in (b). Data is shown on the left while the model that was fit to that data is on the right. (b) The top panel is the low-temperature, single-photon power internal quality factors extracted from all resonators that we measured, excluding those with fabrication defects. The bottom panel shows the TLS losses extracted from the power and temperature dependence of the internal quality factor for each of the resonators. The colored markers are used to label different resonators for easier comparison with figure 5.

3. Microwave characterization

We fabricate CPW resonators and measure their microwave properties as a function of power and temperature (see details in appendices D and E). The losses of microwave resonators were measured by analyzing the S_{21} scattering response and extracting the linewidth and resonance frequency of each resonance. The different physical mechanisms which contribute to the observed loss rate can be distinguished by varying the applied microwave power and temperature [4]. According to similar studies in literature, we expect dielectric losses due to TLS to be the dominant source of loss in the low temperature and single-photon power regime [11, 12]. In addition to losses from TLS, which scale strongly with applied microwave power, we consider loss mechanisms that do not depend on power. These include temperature-dependent losses due to thermal quasiparticles or due to vortex motion, but also temperature-independent losses, e.g. due to external pair-breaking radiation or parasitic modes within the resonators [12, 17, 40, 41]. Therefore, we include $\delta_{PI}(T)$, a PI loss term, in our model:

$$\frac{1}{Q_{\text{int.fit}}(T,P)} = \frac{1}{Q_{\text{int}}^{\text{TLS.full}}(T,P)} + \delta_{\text{PI}}(T)\,. \tag{1}$$

Other authors have employed this practice in different variants, some explicitly modeling the temperature dependence of PI losses [19, 24], some splitting the total loss into a high-power and a low-power regime [11, 18, 42, 43]. The full expression for our TLS loss model $\frac{1}{Q_{\text{int}}^{\text{TLS.full}}(T,P)}$ is presented in appendix F.

Figure 4(a) compares a measurement of the internal quality factor of one resonator from Wafer **B** to equation (1). The excellent agreement indicates that our model captures the temperature and power dependence of the measured quality factors (see figure 17 in appendix I for the same comparison for

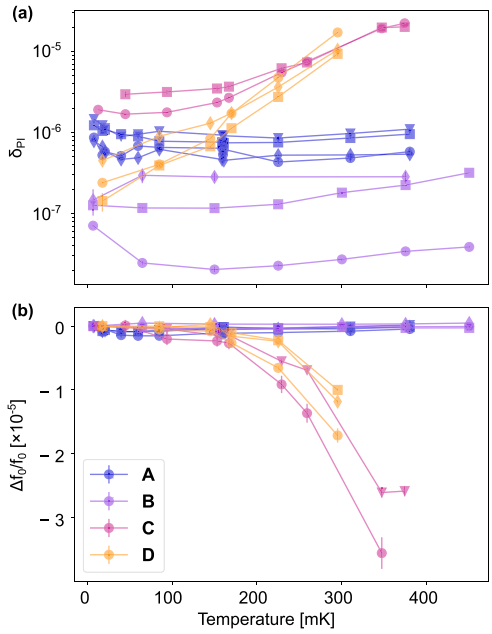

Figure 5. Power-independent loss (a) and fractional frequency shift measured at single-photon power (b) of each resonator measured in figure 4(b) as a function of temperature. The different resonators of each chip from left to right in figure 4(b) are marked in this plot as ●■◆▼.

all resonators shown in figure 4(b)). As predicted by TLS theory, the internal quality factor is highest at high power and has a non-straightforward temperature dependence originating from the competition of TLS saturation and TLS interactions [10, 19, 24]. Additionally, fitting to our model allows us to distinguish TLS loss from PI loss. In figure 4(b) we show the low-temperature single-photon quality factors for each resonator that we measured together with the extracted TLS losses. We excluded any resonators with visible fabrication defects. The yield of high quality factor resonators varied for each chip (see appendix G for details). Resonators from Wafer **B**, grown at 550 K, show substantially higher quality factors and lower TLS losses than resonators grown at the other temperatures. The highest single-photon Q_{int} we measured was $1.1 \pm 0.1 \times 10^6$, which to our knowledge is among the highest ever measured single-photon Q_{int} for a niobium on sapphire resonator [44, 45].

We also fabricated resonators from Wafer **E**, but observed more than one order of magnitude lower internal quality factors than for the other wafers. We attribute this to the high number of defects that exist in wafers grown at 975 K (more detail can be found in appendix H). The formation of these defects is likely a result of surface adhesion problems during film deposition at these high temperatures. We observe only small variations in internal quality factor between Wafers **A**, **C**, and **D** that are on the order of variations between resonators from the same wafer.

The fitted PI losses are shown as a function of temperature in figure 5(a) (for a detailed description of our fitting procedure, see appendix I). We observe a clear temperature dependence of the PI loss for Wafers **C** and **D** while the PI loss appears constant for Wafers **A** and **B**. We further observe differences in the temperature-independent contribution to δ_{PI} that we attribute to slight differences in the measurement environment. These differences are rather small compared to the temperature-dependent variations and compared to the loss from TLS. In figure 5(b), the temperature dependence of the fractional frequency shift $\Delta f_{\mathrm{r}}/f_0 = (f_{\mathrm{r}}(T) - f_{\mathrm{r}}(T \approx 0))/f_{\mathrm{r}}(T \approx 0)$ shows a similar trend, where f_{r} is the resonator frequency extracted from fitting the raw data. This behavior will be further explored in the discussion section. The PI losses are smaller than the TLS losses for resonators from the Wafers **A** and **B** at all temperatures. For Wafers **C** and **D**, we observe that the PI loss dominates over the TLS loss at the highest temperatures that we measured.

The differences that we observed between microwave measurements of our wafers can be interpreted within the context of material properties of our films presented in figure 1. Our XRD characterization shows that the biggest change in crystallinity occurs between Wafers **A** and **B** and that comparatively little change occurs between Wafers **C** and **D**. This interpretation of the XRD data is in line with the values of l_{MFP} and $\xi_{\mathrm{GL}}(0)$ shown in table 2 which indicate that grain boundaries become less frequent in Wafers grown at larger temperatures. The AFM data displayed in figure 2 demonstrates a less straightforward trend, but we can clearly see that Wafer **B** has a far lower surface roughness than the other films.

This could be attributed to the observation that only the niobium film on Wafer **B** is primarily oriented in [110] direction while Wafers **C** and **D** are dominantly oriented in the [111] direction.

The power-dependent response of our resonators indicates that the dominant mechanism limiting our single-photon-power low-temperature internal quality factors is loss due to TLS. We achieve the lowest TLS loss for Wafer **B**, which features the lowest surface roughness, suggesting that the roughness of the film has an effect on TLS loss. The exact mechanism that describes how surface morphology affects the TLS loss in our study is unclear. In films with larger surface roughness, we speculate that the TLS loss could be higher due to an increased volume of dielectric material or the presence of sharp surface features that concentrate the electrical field distribution at the surface. Furthermore, changes in surface morphology observed in the AFM or different dominant crystal orientations could favor the growth of one niobium oxide species over another. This is a critical point, as recent studies have demonstrated that surface oxides of niobium are the dominant source of TLS loss in superconducting circuits [11, 12, 22, 24, 45, 46]. As far as we know, the link between the crystal properties of niobium and the resulting surface oxide thickness and composition has not yet been established.

It is however premature to correlate dielectric loss exclusively with the roughness of a film. For instance, changes in surface roughness between Wafers **C** and **D** are not clearly reflected in their dielectric losses. Furthermore, the average TLS loss of Wafer **A** is 1.5 times that of Wafer **D**, even though Wafer **D** shows a slightly higher surface roughness. We also note that these observations are based on a single wafer for each growth temperature, and their robustness and reproducibility need to be investigated in further work. Nevertheless, taken at face value, one can speculate that there is a separate contribution to the overall TLS loss that depends on grain structure. Oxides are known to penetrate metallic films along grain boundaries [47], potentially hosting additional TLS. Furthermore, disorder in the crystal due to the grain boundaries themselves could also lead to higher TLS loss [10]. In contrast, contributions from other common sources of TLS such as the substrate–air and metal–substrate interfaces are likely negligible in our study from qualitative arguments. The substrate–air interface is completely unchanged between different chips and we have observed no signs of significant interfacial oxides or structural damage of the metal–substrate interface in our STEM study for both high and low-temperature depositions.

Other authors who investigated the effect of different growth conditions on microwave dissipation report higher internal quality factors/T1 times for growths at 770 K [26] or at 1070 K [25] compared to room-temperature growths. Furthermore, in other material systems, highly ordered films displayed lower losses than granular films [15]. Both types of studies only compared the extremes of a continuous spectrum of growth conditions and grain structures. Our results do not contradict these findings, instead, we report a temperature 'sweet spot' in our growth series where the combination of all the factors that affect TLS loss produces the highest low-energy quality factors.

We can also interpret the temperature-dependent behavior in order to investigate PI loss in our resonators. In figure 5, we see that resonators from Wafers **C** and **D** exhibit larger PI loss and a negative frequency shift as temperature is increased. The behavior we observe is consistent with both loss due to thermally populated quasiparticles and loss due to the microwave response of trapped flux vortices [4, 48, 49]. A notable feature of figure 5 is that the temperature-dependent phenomenon is more pronounced for Wafers **C** and **D** than for **A** and **B**. Because our XRD (figure 1) and DC transport (table 2) characterization have established that films of Wafers **C** and **D** have larger crystal domains than those of Wafers **A** and **B**, we suspect that the temperature-dependent phenomena result from the crystal properties of the superconductor. Smaller crystal domains result in a higher density of grain boundaries which can serve as vortex pinning sites, meaning that we would expect a larger amount of trapped vortices in Wafers **A** and **B** than **C** and **D**. Figure 7 also directly reflects stronger vortex pinning from Wafers **A** and **B** which can be seen from the increased $B_{c2}(T)$ values compared to Wafers **C** and **D**. Both possible PI loss mechanisms are influenced by changing the amount of pinned magnetic vortices: vortices trap quasiparticles which mitigates losses that scale with quasiparticle density [50, 51] and fewer pinned vortices have been shown to increase microwave loss related to vortex movement in superconducting circuits [52, 53]. Therefore, we were not able to distinguish between the two with our measurements.

4. Conclusions

In the first section of our study, we show that the crystallographic structure of Nb on sapphire films is drastically affected by changing the deposition temperature. This resulted in films ranging from a poly-crystalline structure (Sample **A**) at room temperature to a completely mono-crystalline character at the highest temperature of 975 K (Sample **E**). With increasing temperature, the films have fewer grain

boundaries and the crystal domains undergo an increasing degree of ordering in the preferred [111] orientation. These differences in crystallinity also lead to variation in surface roughness, most notably in Wafer **B**, which has the lowest surface roughness.

These differences in material properties are correlated with significant variations in the microwave behavior of our superconducting resonators. Specifically, we found the best single-photon quality factors of over one million in the resonators made from Wafer **B**, which was grown at an intermediate temperature of 550 K. These quality factors are state-of-the-art for Nb on sapphire resonators [44, 45], and are within an order of magnitude of the state-of-the-art for niobium resonators on any substrate [12]. We believe that the TLS loss rate could be further reduced by optimizing the fabrication process by including steps like a HF etch to remove the processing oxide [11, 12, 24], etching trenches [42, 54, 55], encapsulating the resonator [23, 56], or optimizing the CPW geometry for low electric field participation at material interfaces [42, 55, 57]. Our results could also be strengthened by measuring more resonators on more samples, as the TLS losses we report vary from resonator to resonator. Nevertheless, they already suggest that the growth temperature could have an important effect on the quality factor of superconducting resonators. In particular, they indicate that TLS losses in Nb qubits on sapphire are reduced by increasing the substrate temperature by only 250 K above room temperature. A similar optimum might also exist for other material systems and are a subject for further investigation. Growing at moderate temperatures will significantly decrease the number of grain boundaries in the film while also leading to relatively low surface roughness. Our work indicates that these factors could reduce the TLS losses by up to an order of magnitude. A relatively small temperature increase during growth could be applied in many different sputtering systems, since it does not put as stringent requirements on the amount of background impurities in the system as the high-temperature growth of, for example, Wafer **D** does.

We also observe a temperature dependence in our resonator measurements that we attribute to the degree of crystallinity of the films. Our data displays two distinct behavioral regimes, which we suspect arise from the relation between the grain boundary density, the resulting density of pinned vortices and their effect on thermal quasiparticle trapping and magnetic vortex motion. The finding, that there exists a grain boundary density below which temperature-dependent losses are strongly suppressed may be relevant for the design of any devices meant to operate above 100 mK. This could further be an important consideration for studying quasiparticle trapping dynamics and microwave losses from magnetic vortices, and motivates future experiments, especially those with a magnetic field degree of freedom. Finally, in the future, this work would benefit from a complimentary study using x-ray photoelectron spectroscopy (XPS) and TEM electron-energy-loss spectroscopy (EELS) analysis to determine the exact thickness and composition of the surface oxide for each wafer. Current research indicates that a specific niobium oxide species, Nb_2O_5 [11, 12, 22, 46] or hydrocarbon contamination [24, 45] can be the dominant source of TLS loss in similar resonator measurements. Establishing the relationship between how the thin film crystal structure and grain boundary density affects the surface oxides of niobium could lead to new techniques for mitigating TLS loss in superconducting circuits.

Data availability statement

The data that support the findings of this study are openly available at the following URL/DOI: https://zenodo.org/records/15979909 [58].

Acknowledgment

We thank M Bahrami Panah, I Kladarić, H Doeleman, T Schatteburg, L Michaud, E Planz, S Andresen, and Y Yang for valuable discussions, ScopeM and specifically P Zeng for lamella preparation by FIB and TEM support and M Sousa (IBM) via the Binning and Rohrer Nanotechnology Center (BRNC) for TEM support. **Funding:** This project has received funding from the European Research Council (ERC) under the European Union's Horizon 2020 research and innovation programme (Grant Agreement No. 948047). This project was additionally supported by the Swiss National Science Foundation (SNSF), Czech Science Foundation (Grant No. 22-22000 M), MEYS CR Grant Nr. CZ.02.01.01/00/22_008/0004594, and Czech Academy of Sciences (Project No. LQ100102201).
Author contribution: M D, S T, and F F conceived the experiment. S T grew the wafers with technical support from C T. S T, F K, D K, and C M performed and analyzed the XRD measurements. S T and F K preformed and analyzed the STEM measurements. S T and F F characterized the wafers using DC transport and AFM measurements. I R and F F

designed the resonators. M D fabricated and packaged the devices. M D and I R constructed the microwave measurement setup. M D and F F performed the microwave measurements. F F performed the fitting and analyzed the data with support from M D and I R. M D, S T, F F interpreted the results and wrote the manuscript, which was revised by all authors. The work was supervised by Y C and W W.

Appendix A. Thin film growth

The Nb thin films were sputtered in an ultra high vacuum (UHV) deposition chamber using DC magnetron sputtering [35]. The films were grown on epi-ready 420 um thick, (0001) sapphire wafers with a diameter of 2 inches. The substrates were pre-baked at 500 K for 8 h in the load lock and subsequently outgassed for 20 min at growth temperature in the UHV chamber before growth. The base pressure of the sputtering chamber was below 2×10^{-10} mBar, indicating a low impurity background. The pressure during the deposition was 8.8×10^{-3} mBar and the distance between the 2 inch Nb target and the substrate was 110 mm. The power applied was 125 W corresponding to a stable sputtering rate of 0.27 nm s^{-1} at room temperature determined from *in-situ* quartz crystal microbalance measurements. The effective growth rate decreased linearly with increasing temperature due to partial re-evaporation of adatoms from the surface. After growth, the thickness was recalibrated using profilometry and TEM measurements and the growth time was adjusted to achieve a thickness of around 185 ± 15 nm for all films. This thickness was chosen to be larger than the London penetration depth at $T = 0$ [59]. The substrate temperature shown in table 1 was set based on pyrometer readings of the temperature of the middle of the wafer.

Appendix B. XRD measurements

In the XRD radial scans, shown in figure 1(a), there are peaks which correspond to the crystal orientations of the niobium film and the sapphire substrate. The substrate peak around 20° corresponds to a nominally forbidden Bragg peak of sapphire and likely shows up in our measurements due to a multiple diffraction (also termed Umweganregung). This is also the reason that, in contrast to the allowed substrate Bragg peaks at around 41° and 91° (the 006 and 0012 Bragg peaks) we observe a strong change in intensity. Such multiple diffraction effects depend sensitively on the sample azimuth which was, however, not controlled for these measurements. Therefore, it is not abnormal to have varying peak heights for these peaks in different XRD measurements.

Additionally, in figure 6 we show linear scales of the 110 (b) and 222 (c) peaks to further assess shifting of the peaks. We note that the shifting of the 222 peak plotted in figure (c) is likely related to a varying degree of strain between the Nb film and substrate. We associate the satellite peak in wafer D with the in-plane misaligned domains that can also be seen in the polefigure of the main text.

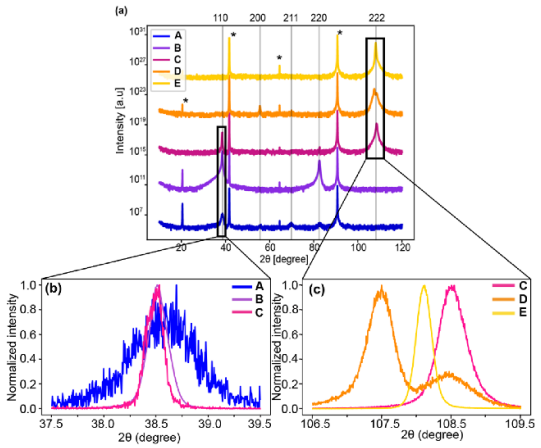

Figure 6. (a) Radial XRD scans discussed in the main text on a logarithmic scale, as well as regions around the 110 peak (b) and 222 peak (c) on a linear scale.

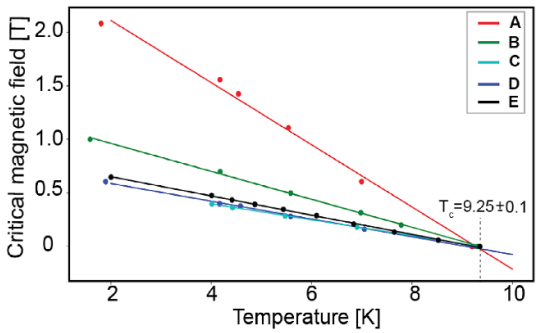

Figure 7. DC low-temperature superconducting characteristics of the our films as a function of temperature and magnetic field. The critical temperature T_C is indicated as the point at which the upper critical magnetic field is zero and is the same for all films.

Appendix C. DC transport characterization

The full data set from which the values for $\xi_{GL}(0)$ shown in table 2 are calculated is plotted in figure 7. Measurements were done at liquid helium temperatures in the Van der Pauw geometry using lock-in amplifiers to measure the relatively low resistances of the films. The bias current was set to 20 μA in order to get good signal-to-noise ratios (SNRs). The critical temperature found for all five wafers was around 9.25 ± 0.1 K.

The out-of-plane critical magnetic field at zero K was determined directly from our data by using the Werthamer–Helfand–Hohenberg relation [60],

$$B_{c2}(0) = 0.69 T_c \left.\frac{dB_{c2}}{dT}\right|_{T=T_c}. \tag{C1}$$

We then calculate a magnetic coherence length using the Ginzburg–Landau (GL) relation at zero temperature:

$$B_{c2}(T) = \frac{\phi_o}{2\pi \xi_{GL}^2(T)}. \tag{C2}$$

This coherence length is not the GL coherence length, as it is determined at temperatures where GL theory is no longer valid. However, it is common practice to report the value of this alternative coherence length in similar studies [35, 39]. We also determine the Fuchs–Sonderheimer mean free path from the wafer's resistivity at 10 K, based on the relationship

$$\rho\ell = \text{const.} \tag{C3}$$

The value of the material constant is based on an idealized assumption from first principle calculations, with $\rho\ell = 3.72 \times 10^{-6} \mu\Omega\text{cm}^2$ [61]. We note that this theory applies to mono-crystalline films as it does not account for grain boundaries or other crystalline defects and thus this mean free path metric may not be accurate for the polycrystalline films shown in table 2.

Appendix D. Device design and fabrication

The design of our CPW resonator chips features four open-circuit $\lambda/2$-resonators of different lengths which are coupled to a central waveguide in the 'hanger' or 'notch' geometry [62, 63]. A single CPW resonator consists of a center conductor of width w_{cc} separated from a lateral ground plane by trenches of width w_{gap}, as illustrated in figure 8. Our chip design features four open-circuit $\lambda/2$-resonators of lengths l_i for $i = 1-4$ and one common feedline, contained in a 10 mm $\times$ 10 mm square chip. Each resonator is of a different length to separate their response in frequency space and to allow the measurement of all four resonators with one read-out signal. A length $l_{\text{coupling}.i}$ of each resonator runs in parallel to the feedline, separated by a distance d_{coupling}. In this layout, each resonator is coupled capacitively to the common feedline, with the coupling strength being controlled by varying $l_{\text{coupling}.i}$ and d_{coupling}. For all chips, $w_{cc} = 10\,\mu$m, $w_{\text{gap}} = 6\,\mu$m, $d_{\text{coupling}} = 12\,\mu$m, and $l_i = (8.782, 8.160, 7.609, 7.120)$ mm are kept constant between different chips.

For this choice of l_i, we determined resonance frequencies of $(7, 7.5, 8, 8.5)$ GHz by simulating our design using AnsysEM. We vary the coupling length $l_{\text{coupling}.i}$ in a range of $25\,\mu$m$-350\,\mu$m between

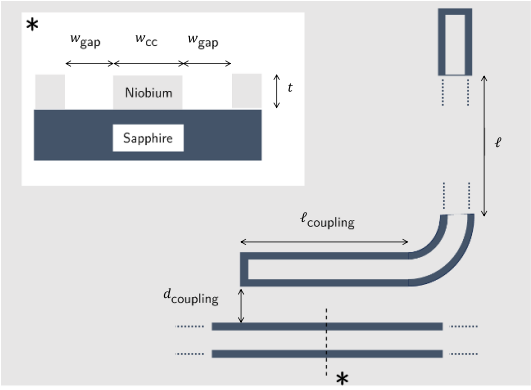

Figure 8. (a) A diagram with the important geometrical parameters in our chip design.

different chips and also within each chip. As a result, we measured coupling quality factors of $Q_c \approx 4 \times 10^4 - 4 \times 10^6$. Internal quality factors can only be determined with small error bars if they are within the critical coupling regime [64] $Q_{int} \sim Q_c$ (see appendix I). In our chip design, each resonator is coupled to the feedline with a different $l_{coupling.i}$ such that the chip covers a broad range of possible internal quality factors. As a consequence, one resonator on Wafer **B** was overcoupled at slightly elevated powers and one resonator on Wafer **D** was overcoupled at all powers. When overcoupled an accurate estimate of the internal quality factors was not possible.

After growth, the 2 inch wafers were diced into quarters for further processing. One quarter was further diced into 5×5 mm chips which were used for AFM, XRD, and the DC transport measurements. The rest of the processing was done on one of the remaining quarters of the wafer, which we refer to here as a sample. At the end of fabrication, each sample is diced into three 10×10 mm chips, one of which was selected for microwave measurements.

The samples are cleaned by being sonicated in acetone and then in isopropanol for two minutes each. Then the samples are baked at 180 °C in the cleanroom air atmosphere for two minutes before we spin a ∼1.5 μm thick layer of AZ 5214E-JP image-reversal photoresist and bake at 105° C for one minute. We use an i-line soft contact masked photolithography process to expose the samples and develop the resist in AZ 726 MIF for three minutes.

After rinsing in water and drying, we load the samples into an Oxford Instruments Plasmalab 80 Plus reactive-ion etcher. We flow five sccm of SF_6 and use an RF power of 100 W while illuminating the sample with a helium-neon laser and monitoring the intensity of the reflected spot. When the intensity of the spot drops (typically after five minutes of etching), we continue etching the samples for between 20 and 75 s in order to account for any anisotropy of the plasma. The dimensions of the resonators (as measured in an optical microscope) were not changed between the 20 and 75 s overetch process. Subsequent STEM measurements of cross-sections of these resonators demonstrate that the sidewall profile of this procedure is consistent between samples.

After etching, the excess resist is stripped in 70 °C n-methyl-2-pyrrolidone (NMP) for at least 30 min before the samples were sonicated in NMP, then acetone, and finally isopropanol for one minute each and blown dry. A Disco DAD 3221 Dicing Saw is used to cut the sample into 10×10 mm chips. We use small pieces of a 100 μm indium sheet to press our chip onto the corner pedestals of a QCage.24 sample holder from Quantum Machines and use aluminum wirebonds to connect the waveguide launchers to the transmission line of the package.

In the context of our conclusions regarding the effect of crystal structure on the microwave properties of our resonators, it is crucial to verify that our fabrication process was reproducible and did not lead to any unwanted variation in the measured resonators. Although effort was made to perform the fabrication process exactly the same for each chip, small variations in for example thickness of the films did require slightly different dry etching times. We show the cross-section of the etched trench for Wafers **A** and **B** in figure 9. From this figure, it can be seen that a very similar etch profile is obtained in both chips. This result further substantiates that the fabrication process was indeed reproducible and the observed differences in microwave characterization are indeed related to the crystal structure rather than chip-to-chip variation in fabrication.

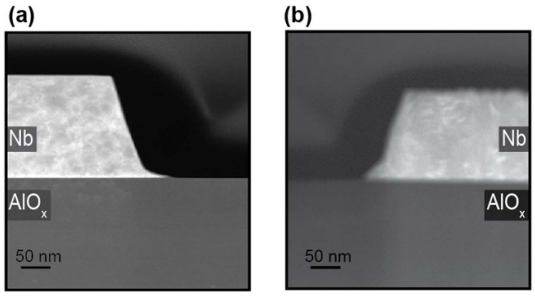

Figure 9. BF STEM images showing the cross-sectional profile of resonators after fabrication from Wafer **B**(a) and Wafer **A**(b).

Appendix E. Microwave measurement details

We conduct microwave measurements in a dilution refrigerator. Our sample is thermalized to the base plate of the cryostat. The temperature of our sample is estimated from a thermometer on the base plate of the cryostat. The microwave response of the resonators is analyzed with a vector network analyzer (VNA) (*Keysight*, P5004A). During the microwave characterization of our samples, we apply microwave signals with powers ranging from −80 dBm to 10 dBm at frequencies between 1 GHz and 12 GHz and record the magnitude and phase of the transmitted signal. We repeat this procedure at temperatures between (8mK, 400mK). Some measurements were repeated to check that the samples were well-thermalized and that the results were reproducible.

The input signal enters the fridge and is subject to 60 dB of attenuation installed on different stages of the cryostat as well as a low-pass filter (*K&L Microwave*, 6L250-12 000/T26000-OP/O) and an eccosorb filter (*Laird*, Eccosorb CR-110) before reaching the sample. The sample and eccosorb filter are inside of a mu-metal magnetic shield (*Amuneal*, A4K Can). After the sample, the signal passes through another eccosorb and low-pass filter as well as two isolators (*LNF*, ISISC4-12A) in series mounted at the mixing chamber plate. The output signal is further amplified at the 4 K stage by a high electron mobility transistor (HEMT) amplifier in addition to a room-temperature amplifier.

In addition to the attenuation from the attenuators, the applied microwave power is further reduced by loss in the cables and attenuation due to microwave reflection at the connectors. To find the total attenuation of the input line we perform a power calibration measurement [65]. While measuring over a broad bandwidth of several gigahertz, we assume that the the noise of the detected signal is dominated by the HEMT amplifier thermal noise. We calculate $P_{\mathrm{HEMT.0\ dBm}}$, the signal power at the HEMT amplifier while applying 0 dBm, by multiplying the noise power of the HEMT amplifier (expressed as a noise RMS voltage) with the SNR of the measured signal at 0 dBm of applied power. Assuming a 50 Ω impedance,

$$\begin{aligned} P_{\mathrm{HEMT.0\ dBm}} &= 10\log\left[\frac{\left(V^{\mathrm{HEMT}}_{\mathrm{Noise\ RMS}} * \mathrm{SNR}_{0\ \mathrm{dBm}}\right)^2}{50/1000}\right] \\ V^{\mathrm{HEMT}}_{\mathrm{noise\ RMS}} &= \sqrt{P_{\mathrm{Noise.HEMT}} * 50} \\ P_{\mathrm{Noise.HEMT}} &= k_{\mathrm{B}} T_{\mathrm{HEMT}} \Delta f. \end{aligned} \tag{E1}$$

We take noise of the HEMT amplifier $P_{\mathrm{Noise.HEMT}}$ from the noise temperature ($T_{\mathrm{HEMT}} = 2$ K) stated in the datasheet of the amplifier. The intermediate frequency bandwidth Δf is set when measuring with the VNA and in our case was 5 kHz. The SNR is calculated by measuring the magnitude of the S_{21} response of a selected frequency range 50 times and dividing the average signal by the standard deviation. By assuming another 2 dB of attenuation between the HEMT amplifier and the sample caused by installed circulators, we find the signal power at the sample to be:

$$P_{\mathrm{on\ chip}}\,[\mathrm{dBm}] = 2\mathrm{dB} + P_{\mathrm{HEMT.0\ dBm}} + P_{\mathrm{applied}}. \tag{E2}$$

The attenuation is given by:

$$\mathrm{Att}\,[\mathrm{dB}] = P_{\mathrm{on\ chip}} - P_{\mathrm{applied}}. \tag{E3}$$

Appendix F. Microwave loss model

From the standard tunneling model [66, 67], the temperature and power dependence of the internal quality factor due to TLS loss can be described by [68]

$$\frac{1}{Q_{\mathrm{int}}^{\mathrm{TLS}}} = \delta_{\mathrm{Loss.TLS}} \frac{\tanh\left(\frac{\hbar\omega_r}{2k_{\mathrm{B}}T}\right)}{\sqrt{1+\frac{n_{\mathrm{ph}}^{\alpha}(P)}{n_{\mathrm{s}}(T)}}} \tag{F1}$$

where $\delta_{\mathrm{Loss.TLS}} = \sum_i^N p_i \delta_{\mathrm{TLS}.i}$ is the sum over different lossy regions i, each with loss tangent $\delta_{\mathrm{TLS.i}}$ and participation ratio p_i. The participation ratio of a volume i is the fraction of the total electric field strength concentrated in that volume $p_i = \int_{V_i} \frac{\epsilon_i}{2} |\mathbf{E}_i(\mathbf{r})|^2 / E_{\mathrm{tot}}\, \mathrm{d}\mathbf{r}$ [36]. $n_{\mathrm{ph}}(P)$ is the power-dependent intracavity photon number, α is a fitting parameter that is introduced to account for the effect of non-uniform field distributions over the length of the transmission line that makes up the resonator [24, 69], $\omega_r = 2\pi f_{\mathrm{r}}$ is the angular resonance frequency of the resonator and $n_{\mathrm{s}}(T)$ is the photon number at which the TLS saturate.

We cannot quantitatively distinguish between the contributions of different dielectrics to our total loss in this study. To isolate loss contributions from different interfaces (e.g. the substrate-air interface), we would need to vary the cross-sectional geometry of our resonators [4], while to differentiate between loss contributions from different dielectric materials we would need to identify the dielectric species present on each wafer by means of XPS or EELS [11]. Therefore, we only fit the overall sum of dielectric losses $\delta_{\mathrm{Loss.TLS}}$ in our model. This description is still sufficient in our case, as we have qualitative arguments to exclude contributions of different interfaces (see the penultimate paragraph of the Results and Discussion section.

The saturation photon number $n_{\mathrm{s}}(T)$ is proportional to $(\tau_1(T)\tau_2(T))^{-1}$, the inverse of the averaged relaxation and decoherence times of the TLS ensemble [19, 24, 70]. According to the spin-boson model, we expect the relaxation time to follow a thermal distribution $\tau_1 \propto \tanh\left(\frac{\hbar\omega_r}{2k_{\mathrm{B}}T}\right)$, while we model decoherence from TLS-TLS and TLS-phonon interactions as a simple inverse polynomial relation $\tau_2 \propto T^{-\beta}$ [19, 24, 68, 71]. This yields the expression $n_{\mathrm{s}}(T) \approx DT^{\beta} \coth\left(\frac{\hbar\omega_r}{2k_{\mathrm{B}}T}\right)$ which describes the temperature dependence of the saturation photon number. Our TLS model (equation (F2)) includes four fit parameters: the exponents α and β, a proportionality constant of the saturation photon number D, and the TLS loss $\delta_{\mathrm{Loss.TLS}}$ [24]:

$$\frac{1}{Q_{\mathrm{int}}^{\mathrm{TLS.full}}} = \delta_{\mathrm{Loss.TLS}} \frac{\tanh\left(\frac{\hbar\omega_r}{2k_{\mathrm{B}}T}\right)}{\sqrt{1+\frac{n_{\mathrm{ph}}^{\alpha}(P)}{DT^{\beta}}\tanh\left(\frac{\hbar\omega_r}{2k_{\mathrm{B}}T}\right)}}. \tag{F2}$$

To model PI but potentially temperature-dependent losses besides TLS loss, we introduce a fifth, temperature-dependent fitting parameter δ_{PI}, resulting in our final loss model:

$$\frac{1}{Q_{\mathrm{int.fit}}(T,P)} = \frac{1}{Q_{\mathrm{int}}^{\mathrm{TLS.full}}(T,P)} + \delta_{\mathrm{PI}}(T). \tag{F3}$$

To apply equation (F3) to our data, we need to determine the photon number in the resonator $n_{\mathrm{ph}}(P)$ as a function of applied microwave power. We can convert microwave power to photon number using the expression [69, 72]

$$n_{\mathrm{ph}} = \frac{P_{\mathrm{in}}}{hf_{\mathrm{r}}^2}, \tag{F4}$$

where h is the Planck constant. The power in the resonator P_{in}, also referred to as the 'circulating power', can be derived from input-output theory [73] to be given as [69, 72]

$$P_{\mathrm{in}} = P_{\mathrm{on\ chip}} \frac{Q_{\mathrm{int}}^2 Q_{\mathrm{c}}}{\pi (Q_{\mathrm{int}} + Q_{\mathrm{c}})^2}, \tag{F5}$$

where $P_{\text{on chip}}$ is the applied power after attenuation. In cases where the response of the resonator shows duffing behavior a different formalism for the calculation of the photon number in the resonator is used (see appendix I).

We did not model the effect of dielectric loss on the resonance frequency, because the accuracy of our frequency measurements and fitting procedure was only sufficient to resolve relatively large frequency shifts (on the order of $\Delta f_r/f_0 \approx 10^{-5}$, likely caused by excess quasiparticles) but was not sufficient to resolve the comparably smaller fractional frequency shifts caused by TLS (which are on the order of $\Delta f_r/f_0 \approx 10^{-6}$ [17, 24]).

Appendix G. Device overview

Over the course of this experiment we measured five samples, each of which had four resonators. In table 3, we show the frequencies and external and internal quality factors of all of our measurements. The resonators in the table are sorted by frequency. We were able to measure all of the resonators except for one on Wafer **E**. We indicate the number of resonators with visible defects for each wafer and which resonators were not included in figures 4(b) and 5. In figure 10, we reproduce figure 4(b) including all resonators that we measured (plotted on a logarithmic scale for clarity).

We chose not to include the data for several resonators in the main text due to specific reasons indicating that they do not give useful information about the relationship between film properties and resonator quality factors. We suspect that the low internal quality factors of three resonators on Wafers **B** and **C** are related to fabrication imperfections, which were visible upon inspection of the device. Resonator 4 on Wafer **D** had a low external quality factor (by design) that made the fit to our loss model fail despite a high internal quality factor. We attribute the low internal quality factors measured on Wafer **E** to visible growth defects, which are further discussed in appendix H.

We further want to point out the large difference between the internal and external quality factors of resonator 4 on Wafer **B**. As the internal quality factor increases with applied microwave power, this resonator's internal quality factor increased beyond the critical coupling regime already at only slightly increased powers. This resonator was not as strongly overcoupled as resonator 4 of Wafer **D** and therefore yielded a few reliable data points at low powers, however, this still lead to large error bars in the fitted TLS-loss shown in figure 4(b).

Table 3. All resonator measurements from each wafer. ♠ indicates resonators not included in figures 4(b) and 5.

	Wafer **A**	Wafer **B**	Wafer **C**	Wafer **D**	Wafer **E**
Resonator 1		♠			Not found
f_0 (GHz)	6.9	6.3	4.6	7.1	
Q_{int} $[\cdot 10^3]$	340 ± 50	2.0 ± 0.1	360 ± 20	450 ± 80	
Q_{ext} $[\cdot 10^3]$	4500 ± 300	1.8 ± 0.1	1700 ± 60	2000 ± 30	
Resonator 2			♠		♠
f_0 (GHz)	7.3	7.6	6.1	7.5	10.1
Q_{int} $[\cdot 10^3]$	250 ± 50	940 ± 100	4.2 ± 0.1	270 ± 40	10 ± 1
Q_{ext} $[\cdot 10^3]$	1300 ± 100	1100 ± 70	27 ± 0.4	220 ± 10	36 ± 3
Resonator 3			♠		♠
f_0 (GHz)	7.8	8.2	6.2	8.0	10.5
Q_{int} $[\cdot 10^3]$	230 ± 50	720 ± 100	2.3 ± 0.1	290 ± 50	11 ± 0.6
Q_{ext} $[\cdot 10^3]$	820 ± 70	1500 ± 100	13 ± 0.2	110 ± 7	10 ± 0.3
Resonator 4				♠	♠
f_0 (GHz)	8.3	8.7	8.3	8.3	11.0
Q_{int} $[\cdot 10^3]$	180 ± 30	1100 ± 100	200 ± 4	270 ± 150	8 ± 0.1
Q_{ext} $[\cdot 10^3]$	380 ± 30	350 ± 9	190 ± 2	33 ± 2	2.6 ± 0.1
# of resonators with visible defects	0	1	2	0	4

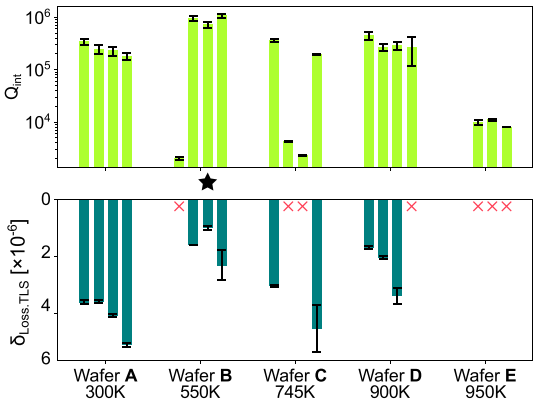

Figure 10. Figure 4(b) from the main text with the quality factors plotted on a logarithmic scale and including all resonators that we were able to measure. The top panel shows the fitted internal quality factors of each resonator while the bottom shows the extracted TLS loss tangent for each resonator. The star indicates the resonator used in figure 4(a) and resonators which we were not able to fit to our loss model are marked with a red ×.

Appendix H. Growth defects at high temperatures

At growth temperatures above 900 K, we observe high densities of point-like growth defects. While the root cause of these defects could not be definitely established, we believe that reduced adhesion of Nb atoms at high growth temperatures is the cause of these defects. Any impurity or defect on the surface of the sapphire substrate can lead to localized spots where the Nb does not nucleate homogeneously and ultimately results in a hole in the film. Alternatively, misfit dislocations originating from the interface with the substrate that arise from an increase in crystal domain size could be a possible explanation.

The density of defects that we observed is always high at high growth temperatures but can vary from wafer to wafer. We observed this variation even though the substrate preparation was the same for all growths. While for wafers of type **D** grown at 900 K we can achieve low defect densities, this was not possible for wafers grown at 975 K (Wafer **E**). For this wafer, even after multiple attempts, the defect density remained high. Resonators that are fabricated on wafers with visibly high defect densities show orders of magnitude lower single-photon power low-temperature internal quality factors (1.0×10^4 and 1.2×10^4 for two resonators on Wafer **E**) compared to our other devices. We exclude these devices from our main study, as the mechanisms limiting them are exclusive for the highest temperatures and no clear trend is visible.

A qualitative comparison of the density of these defects between a high-temperature and a low-temperature wafer is shown in figure 11.

Appendix I. Fitting procedures

I.1. Fitting S_{21} microwave data

We analyze the complex S_{21} scattering matrix element of the microwave signal that is sent through the signal chain. From transmission line theory one can derive the S_{21} response of the equivalent lumped LC-circuit for a notch-type configuration [62, 63]

$$S_{21}^{\text{ideal}} = 1 - \frac{(Q_l/|Q_c|)\,e^{i\phi}}{1+2iQ_l(f/f_r-1)}, \tag{I1}$$

with the loaded quality factor Q_l, the coupling quality factor Q_c, the frequency f, and the resonance frequency f_r. We include asymmetries in the response due to an impedance mismatch in the phase $e^{i\phi}$ of Q_c and fit the phase ϕ [63, 74]. We extend the ideal model by adding a complex prefactor to account for an imperfect background with a cable damping a, a frequency-dependent cable delay τ, and an initial phase offset α [63]

$$S_{21}^{\text{real}} = ae^{i\alpha}e^{-2\pi i f\tau}\left[1 - \frac{(Q_l/|Q_c|)\,e^{i\phi}}{1+2iQ_l(f/f_r-1)}\right]. \tag{I2}$$

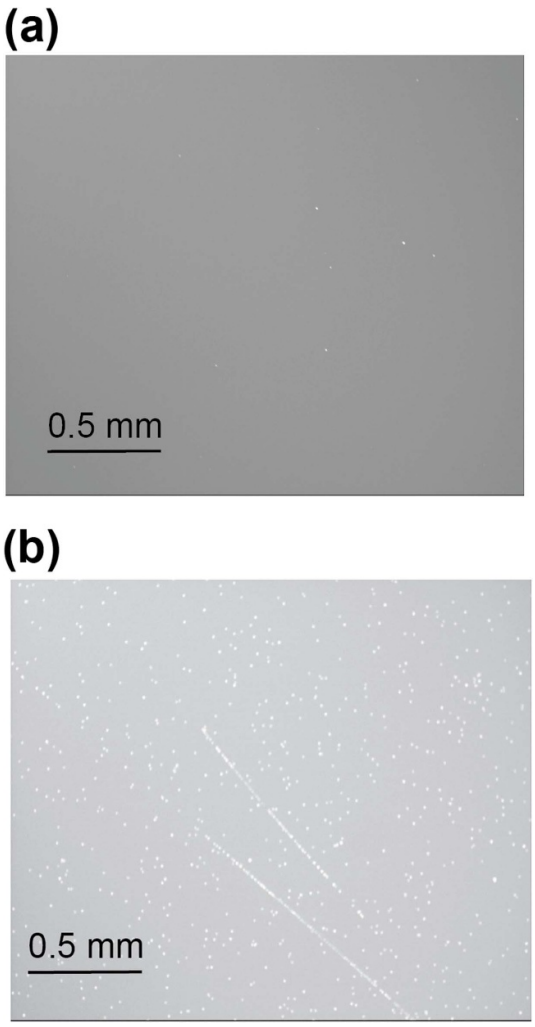

Figure 11. Optical microscope images of adhesion defects. (a) Shows a wafer with low defect density grown at room temperature. (b) Shows a wafer with a very high defect density grown at 975 K.

While Q_c describes energy dissipation into the waveguide through the coupling channel, we are mainly interested in the internal quality factor Q_{int}, which describes all other sources of loss, including material losses. We can determine Q_{int} from the relation $Q_l^{-1} = Q_{int}^{-1} + \Re(Q_c^{-1}) = Q_{int}^{-1} + |Q_c|^{-1}\cos\phi$, following the diameter correction method formalism [74]. By fitting the measured scattering responses with equation (I2), we extract the external and internal quality factors and the resonance frequency of each resonator as a function of temperature and applied microwave power.

We perform a two-step least-squares fit of our data with equation (I2). As a first step, we remove the data around the resonance peak and fit the surrounding background with the expression for the imperfect background in equation (I2). As a second step, we use the parameters of the fitted background as initial guesses and fit the complete model, including a refit of the background parameters. We used a modified version of the stlab [75] fitting routine which employs the Python library lmfit. This method automatically estimates the standard deviation for all of our fits. The individual steps are shown in figure 12.

In figure 13 we show a comparison between the fitted quality factors obtained from the commonly used circle fit method [63] and the direct fitting of equation (I2) for one representative power trace of one resonator from Wafer **B**. Both methods fit the same physical model but with different numerical procedures. The obtained values only differ significantly at the lowest applied powers, where the circle fit method yields a strongly divergent coupling quality factor. Since divergent behavior of Q_c is unphysical, we trust the values obtained by the direct fit more and use the direct fit as our standard fitting procedure.

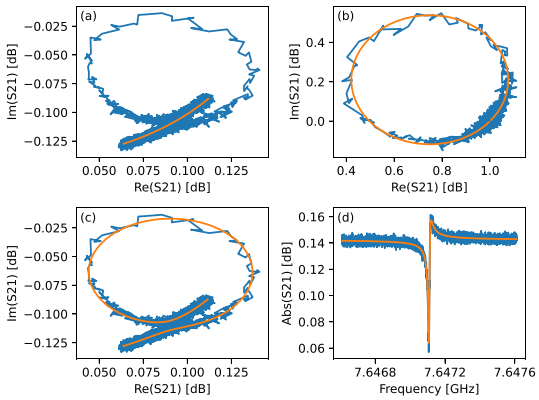

Figure 12. (a) Shows the initial background fit of the resonance circle. (b) Shows the resonance circle with the background removed and the ideal fit. (c) Shows the final fit of the resonance circle including the final background refit. (d) Shows the final fit of the signal magnitude. The data is taken from one resonator of Wafer **B** at −50 dBm applied power.

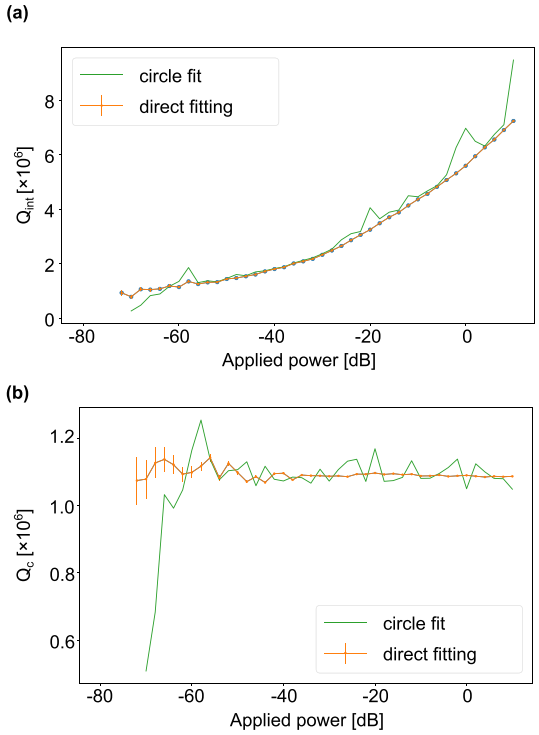

Figure 13. Comparison of the direct fitting routine adapted from [75] to the fitting routine employed by Probst *et al* [63]. (a) Fitted internal quality factor versus power for one resonator from Wafer **B**. (b) Fitted coupling quality factor for the same resonator.

Some resonators show Duffing-type nonlinear behavior at the highest measurement powers that our standard fit was not able to capture (see figure 14). The Duffing-type behavior is likely caused by a Kerr nonlinearity and can be modeled as a shift in the resonance frequency of the resonator with microwave power [76]. This shift is introduced as a squared term in the equation of motion for the mode amplitude [65]:

$$\dot{\alpha} + \left(\mathrm{i}\left(\omega_r + \beta|\alpha|^2\right) + \frac{\kappa}{2}\right)\alpha = 0, \tag{I3}$$

where α is the mode amplitude, β the Kerr anharmonicity, $\kappa = \frac{f_r}{Q_l}$ is the total decay rate. For a derivation of this expression without the anharmonicity term, refer to section 7.2 in [73].

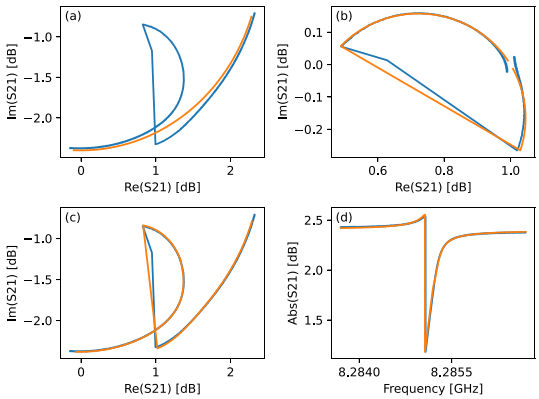

Figure 14. (a)–(d) Show the same fitting routine as displayed in figure 12 but using the nonlinear model from equation (I4). The data is taken from one resonator of Wafer **C** at −26 dBm applied power.

We can express the scattering parameter in terms of the mode amplitude $\alpha = |\alpha| e^{-i\psi}$ with a phase ψ [77]

$$S_{21}^{\text{ideal.duffing}} = 1 + i\sqrt{\frac{\kappa_c}{2}} \frac{|\alpha| e^{-i\psi}}{\sqrt{\Phi_{\text{applied}}}} e^{i\phi}$$
$$\psi = \operatorname{atan2}\left(\frac{2\left(\Delta - \beta|\alpha|^2\right)}{\kappa}\right) \tag{I4}$$

with $e^{i\phi}$ being introduced to account for impedance mismatches, $\Delta = \omega - \omega_r$ and $\Phi_{\text{applied}} = \frac{P_{\text{applied}}}{h f_r}$ the photon number flux due to the power that is applied to the resonator. From the coupling decay rate $\kappa_c = \frac{f_r}{|Q_c|}$ and the total decay rate κ we can determine the internal decay rate $\kappa_{\text{int}} = \frac{f_r}{Q_{\text{int}}}$ by applying again the diameter correction method $\kappa = \kappa_{\text{int}} + \kappa_c \cos\phi$. The mode magnitude is given by $|\alpha| = \sqrt{n_{\text{ph}}}$ where n_{ph} can be found as the smallest real positive root of the mode equation rewritten as a third-order polynomial [65]

$$\beta^2 n_{\text{ph}}^3 - 2\Delta\beta n_{\text{ph}}^2 + \left(\Delta^2 + \frac{\kappa^2}{4}\right) n_{\text{ph}} - \kappa_e \Phi_{\text{applied}} = 0. \tag{I5}$$

For all methods of fitting the S_{21} microwave data, we observe a strong decrease in fit accuracy when the internal quality factor exceeds the external quality factor. For $Q_{\text{int}} \gg Q_c$, the resonator enters the overcoupled regime [64] where coupling losses dominate over internal losses. In this regime the resolution of Q_{int} becomes increasingly low and the uncertainty of the fit increases. For this reason, we excluded fitted internal quality factors for which $Q_{\text{int}} \geqslant 10\ Q_{\text{ext}}$. This was not a problem for Wafers **A** and **C**, however, one resonator of Wafer **B** and one resonator of Wafer **D** could not be fitted for this reason. We note here that measuring in a strongly undercoupled regime $Q_{\text{int}} \ll Q_c$ is not ideal either, as high microwave powers are necessary to introduce photons in the resonator. Driving the whole system at high power renders the system more susceptible to heating and other sources of noise.

At the highest microwave powers that we measured, we observe behavior that is not easily fitted by our standard loss model. The resonance circle starts to appear deformed and/or features jumps due to nonlinear dissipative behavior [78]. If the resonance circle only features a jump, marked as behavior (1) in figure 15, the internal quality factor can still be extracted with equation (I4). If the resonance circle features other distortions, like caving in towards the jump, marked as behavior (2) for −6.0 dB and 0.0 dB in figure 15(a), the fit will return incorrect results as the numerical method tries to fit a regular circle (or in the case of duffing behavior, a regular circle with a jump to the deformed data). Even though it is expected that the internal quality factor decreases at high power [79], the high-power internal quality factors shown in figure 15(b) are likely an underestimation due to the aforementioned fitting errors.

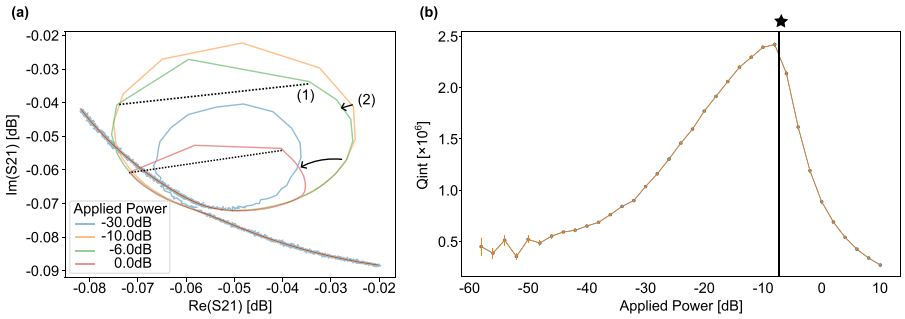

Figure 15. High-power behavior of one resonator from Wafer **D**. In the raw data (a), the resonance circle starts to feature a jump (1) and caves in towards the jump (2) around −6.0 dB. The abrupt jumps (1) are a sign of duffing behavior and can be fitted, however, our fit can not account for the deformation of type (2). In (b) we show the decrease in internal quality factor at the highest powers calculated by our fitting routine. The star marks the onset of behavior (2).

I.2. Fitting of loss models

As described in appendix F, our loss model includes four fitting parameters accounting for TLS loss and one parameter at each temperature that models a PI offset due to other temperature-dependent losses (e.g. for power traces at five temperatures, we fit 4 + 5 parameters). We label the parameters modeling this PI offset as $\delta_{\mathrm{PI}i}$ with i indexing the different temperatures from lowest to highest. We bound the values of the fitting parameters α and β to lie within $(0.001, 1)$ and $(0.001, 2)$ respectively for better convergence. The values of the bounds are based on the results of [19, 24]. A non-linear least-squares fit is performed using the lmfit package in Python. The Q_{int} values the model is fitted to are weighted by their corresponding standard deviation. We do not include internal quality factors data points from the highest powers beyond the point where the internal quality factor starts to decrease (marked with a star in figure 15(b)), as this behavior is not modeled by equation (F3) and, as we argue in the previous section, the fit uncertainty is high. Different sets of initial parameters were swept, and the resulting fits were ranked by minimal overall standard deviation, minimal reduced chi-squared, and minimal overall cross-correlations. In table 4, we report the most relevant metrics of our best fits, as they are output by the fitting function. All our fits converged within a small number of function evaluations, with no parameters on the boundary of the parameter space. Most parameters were determined with a relatively low uncertainty. The cross-correlation parameters for some of our fit parameters were relatively high. This means that the uncertainty we report for these parameters is underestimated. This was especially the case for the normalization constant of the photon number D and the exponent α, which is one reason why we do not interpret their values in our analysis, apart from such an analysis exceeding the scope of our work. These two parameters appear in the relation $\frac{n_{\mathrm{ph}}^{\alpha}(P)}{DT^{\beta}}$ in equation (F2) and are connected to the scaling of $\frac{1}{Q_{\mathrm{int}}^{\mathrm{TLS,full}}}$ with photon number. Since we were not always able to record the full flattening out of the Q_{int}-vs-n_{ph} curve at photon numbers lower than one, we are potentially missing some of the curve shape that would have been necessary to determine these parameters with lower uncertainty. The maximum cross-correlation involving $\delta_{\mathrm{Loss,TLS}}$ was overall lower than between the other parameters. The reduced chi-squared values, while not ideal, are low for most fits, except for the second resonator of Wafer **C**, which did not perform as well. We argue that the chi-squared values are likely overestimated, since the uncertainty we used to normalize the chi-squared metric did not include uncertainty from cross-correlations between the parameters of the S_{21}-data fit. We were unable to find a study in which fit results are reported in as much detail as in our study, so we find it challenging to compare our results. In figure 16, we show a different representation of the data plotted in the color map in figure 4(a). In figure 17, we show the results of fitting the power and temperature-dependent data of all resonators included in figure 4(b).

Table 4. Overview of the fitted parameters used in the fits of the TLS model. The PI loss at each temperature and the TLS loss are shown in figures 4(b) and 5 respectively.

Wafer	f_0 (GHz)	D	α	β	Max. cross-corr.	Max. cross-corr. w. $\delta_{\text{Loss.TLS}}$	Red. χ^2
A	6.9	216 ± 22	0.3864 ± 0.0065	1.206 ± 0.015	D-α: +0.8900	δ_{PI1}-$\delta_{\text{Loss.TLS}}$: −0.8520	54.40
	7.3	48.7 ± 3.8	0.3274 ± 0.0038	1.045 ± 0.014	D-α: +0.8496	D-$\delta_{\text{Loss.TLS}}$: −0.6640	32.56
	7.8	136.1 ± 8.0	0.4078 ± 0.0038	1.118 ± 0.010	D-α: +0.7825	δ_{PI1}-$\delta_{\text{Loss.TLS}}$: −0.6903	32.40
	8.3	166 ± 20	0.3575 ± 0.0063	1.290 ± 0.022	D-α: +0.8734	δ_{PI9}-$\delta_{\text{Loss.TLS}}$: −0.7189	60.29
B	7.6	5.64 ± 0.15	0.3317 ± 0.0015	0.3459 ± 0.0031	D-α: +0.8761	D-$\delta_{\text{Loss.TLS}}$: −0.4846	88.15
	8.2	6.5 ± 1.7	0.589 ± 0.021	0.431 ± 0.019	δ_{PI1}-α: +0.9202	D-$\delta_{\text{Loss.TLS}}$: −0.8988	12.78
	8.7	0.41 ± 0.31	0.994 ± 0.093	0.15 ± 0.11	D-$\delta_{\text{Loss.TLS}}$: -0.8328	D-$\delta_{\text{Loss.TLS}}$: −0.8328	44.53
C	4.6	1.288 ± 0.059	0.1935 ± 0.0046	0.800 ± 0.012	D-α: +0.6441	D-$\delta_{\text{Loss.TLS}}$: −0.3304	3.02
	8.3	3.8 ± 1.5	0.410 ± 0.064	0.73 ± 0.21	δ_{PI4}-$\delta_{\text{PI5}} = +0.9532$	α-$\delta_{\text{Loss.TLS}}$: -0.8995	433.79
D	7.1	49.6 ± 7.8	0.5160 ± 0.0089	0.393 ± 0.026	D-α: +0.8458	D-$\delta_{\text{Loss.TLS}}$: −0.6715	12.33
	7.5	41 ± 11	0.471 ± 0.014	0.398 ± 0.073	δ_{PI1}-β: +0.9199	α-$\delta_{\text{Loss.TLS}}$: −0.6402	35.82
	8.0	7.0 ± 2.5	0.566 ± 0.036	0.123 ± 0.046	D-$\delta_{\text{Loss.TLS}}$: -0.9052	D-$\delta_{\text{Loss.TLS}}$: −0.9052	21.13

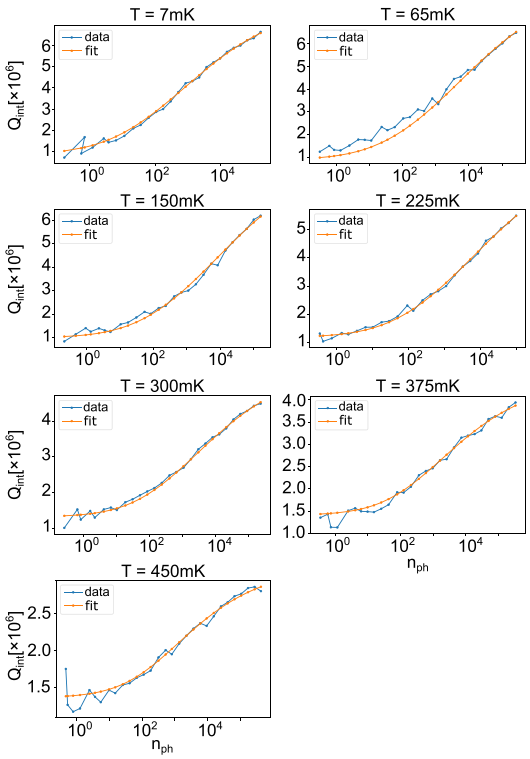

Figure 16. An alternative representation of figure 4(a), showing the employed TLS model fitting power traces at various temperatures.

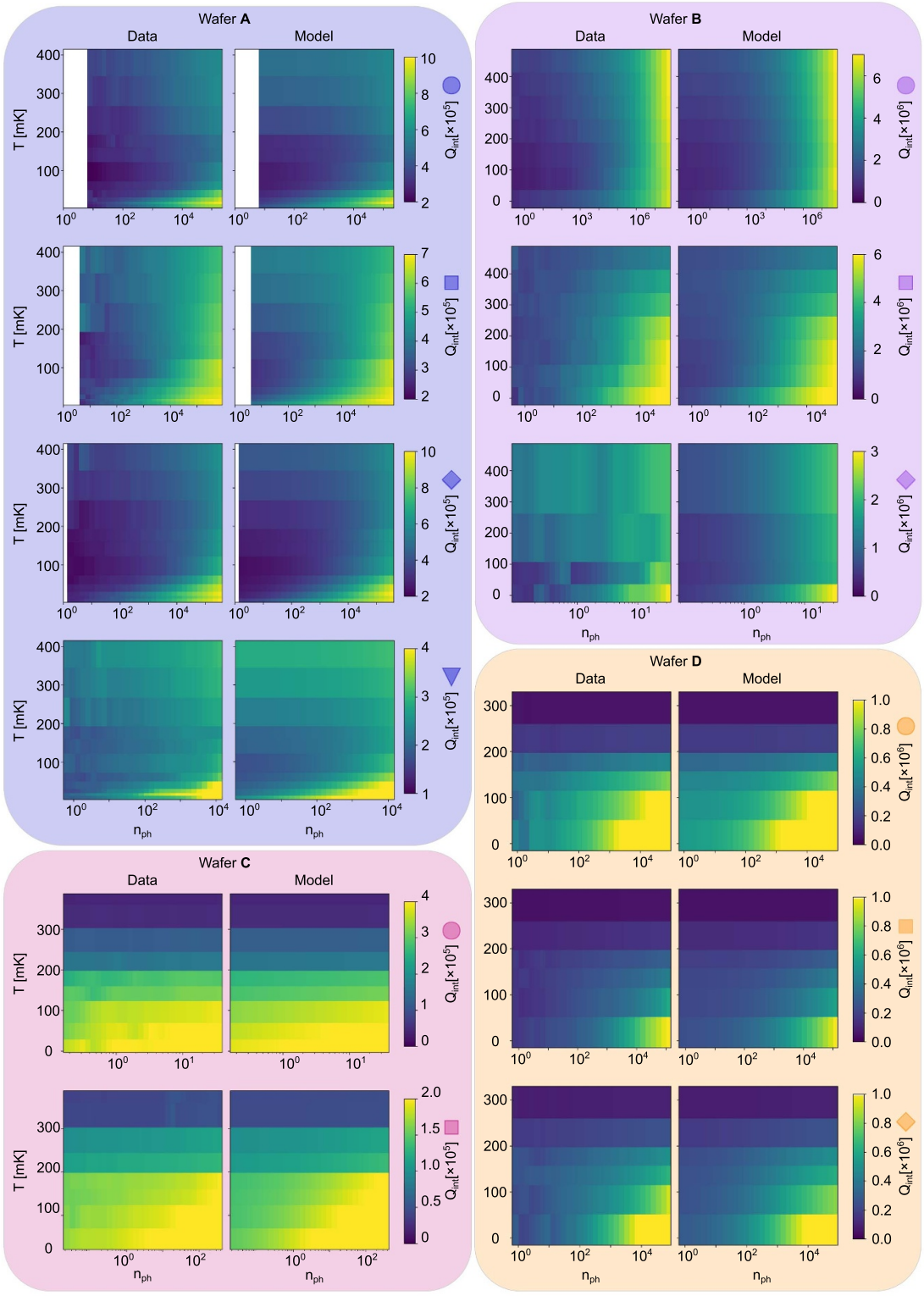

Figure 17. Comparison between data and model for all resonators included in figure 4(b).

ORCID iDs

Maxwell Drimmer 0000-0003-3515-2330
Felix L Fischer 0009-0007-7166-3222
Clemens Todt 0009-0000-9679-2767
Dominik Kriegner 0000-0001-6961-6581
Christoph Müller 0009-0008-4256-3342

References

[1] Murray C E 2021 Material matters in superconducting qubits *Mater. Sci. Eng. R* **146** 100646
[2] Siddiqi I 2021 Engineering high-coherence superconducting qubits *Nat. Rev. Mater.* **6** 875
[3] de Leon N P, Itoh K M, Kim D, Mehta K K, Northup T E, Paik H, Palmer B S, Samarth N, Sangtawesin S and Steuerman D W 2021 Materials challenges and opportunities for quantum computing hardware *Science* **372** eabb2823
[4] McRae C R H, Wang H, Gao J, Vissers M R, Brecht T, Dunsworth A, Pappas D P and Mutus J 2020 Materials loss measurements using superconducting microwave resonators *Rev. Sci. Instrum.* **91** 091101
[5] Aumentado J 2020 Superconducting parametric amplifiers: the state of the art in josephson parametric amplifiers *IEEE Microwave Mag.* **21** 45
[6] de Graaf S E, Danilov A V, Adamyan A and Kubatkin S E 2013 A near-field scanning microwave microscope based on a superconducting resonator for low power measurements *Rev. Sci. Instrum.* **84** 023706
[7] Day P K, LeDuc H G, Mazin B A, Vayonakis A and Zmuidzinas J 2003 A broadband superconducting detector suitable for use in large arrays *Nature* **425** 817
[8] Ulbricht G, De Lucia M and Baldwin E 2021 Applications for microwave kinetic induction detectors in advanced instrumentation *Appl. Sci.* **11** 2671
[9] Kjaergaard M, Schwartz M E, Braumüller J, Krantz P, Wang J I-J, Gustavsson S and Oliver W D 2020 Superconducting qubits: current state of play *Annu. Rev. Condens. Matter Phys.* **11** 369
[10] Müller C, Cole J H and Lisenfeld J 2019 Towards understanding two-level-systems in amorphous solids: insights from quantum circuits *Rep. Prog. Phys.* **82** 124501
[11] Altoé M V P *et al* 2022 Localization and mitigation of loss in niobium superconducting circuits *PRX Quantum* **3** 1
[12] Verjauw J *et al* 2021 Investigation of microwave loss induced by oxide regrowth in high-Q niobium resonators *Phys. Rev. Appl.* **16** 014018
[13] Wisbey D S, Gao J, Vissers M R, da Silva F C S, Kline J S, Vale L and Pappas D P 2010 Effect of metal/substrate interfaces on radio-frequency loss in superconducting coplanar waveguides *J. Appl. Phys.* **108** 093918
[14] Sandberg M, Vissers M R, Kline J S, Weides M, Gao J, Wisbey D S and Pappas D P 2012 Etch induced microwave losses in titanium nitride superconducting resonators *Appl. Phys. Lett.* **100** 262605
[15] Megrant A *et al* 2012 Planar superconducting resonators with internal quality factors above one million *Appl. Phys. Lett.* **100** 113510
[16] Quintana C M *et al* 2014 Characterization and reduction of microfabrication-induced decoherence in superconducting quantum circuits *Appl. Phys. Lett.* **105** 062601
[17] Bruno A, de Lange G, Asaad S, van der Enden K L, Langford N K and DiCarlo L 2015 Reducing intrinsic loss in superconducting resonators by surface treatment and deep etching of silicon substrates *Appl. Phys. Lett.* **106** 182601
[18] Earnest C T, Béjanin J H, McConkey T G, Peters E A, Korinek A, Yuan H and Mariantoni M 2018 Substrate surface engineering for high-quality silicon/aluminum superconducting resonators *Supercond. Sci. Technol.* **31** 125013
[19] Goetz J *et al* 2016 Loss mechanisms in superconducting thin film microwave resonators *J. Appl. Phys.* **119** 015304
[20] Burnett J, Faoro L and Lindström T 2016 Analysis of high quality superconducting resonators: consequences for tls properties in amorphous oxides *Supercond. Sci. Technol.* **29** 044008
[21] Lock E H, Xu P, Kohler T, Camacho L, Prestigiacomo J, Rosen Y J and Osborn K D 2019 Using surface engineering to modulate superconducting coplanar microwave resonator performance *IEEE Trans. Appl. Supercond.* **29** 1
[22] Kowsari D, Zheng K, Monroe J T, Thobaben N J, Du X, Harrington P M, Henriksen E A, Wisbey D S and Murch K W 2021 Fabrication and surface treatment of electron-beam evaporated niobium for low-loss coplanar waveguide resonators *Appl. Phys. Lett.* **119** 132601
[23] Alghadeer M, Banerjee A, Hajr A, Hussein H, Fariborzi H and Rao S G 2023 Surface passivation of niobium superconducting quantum circuits using self-assembled monolayers *ACS Appl. Mater. Interfaces* **15** 2319
[24] Crowley K D *et al* 2023 Disentangling losses in tantalum superconducting circuits *Phys. Rev. X* **13** 041005
[25] Dominjon A, Shu S, Kroug M, Noguchi T, Sekimoto Y, Shan W, Sekiguchi S and Nitta T 2019 Investigation of single-crystal niobium for microwave kinetic inductance detectors *J. Low Temp. Phys.* **194** 404
[26] Place A P M *et al* 2021 New material platform for superconducting transmon qubits with coherence times exceeding 0.3 milliseconds *Nat. Commun.* **12** 1779
[27] Kittel C 2004 *Introduction to Solid State Physics* 8th edn (Wiley) (available at: www.amazon.com/Introduction-Solid-Physics-Charles-Kittel/dp/047141526X/ref=dp_ob_title_bk)
[28] Wildes A R, Mayer J and Theis-Bröhl K 2001 The growth and structure of epitaxial niobium on sapphire *Thin Solid Films* **401** 7
[29] Thornton J A 1988 Structure-zone models of thin films *Model. Opt. Thin Films* **0821** 95
[30] Flynn C P 1988 Constraints on the growth of metallic superlattices *J. Phys. F: Met. Phys.* **18** L195
[31] Sürgers C, Strunk C and Löhneysen H V 1994 Effect of substrate temperature on the microstructure of thin niobium films *Thin Solid Films* **239** 51
[32] Anders A 2010 A structure zone diagram including plasma-based deposition and ion etching *Thin Solid Films* **518** 4087
[33] Edwards J W, Speiser R and Johnston H L 1951 High temperature structure and thermal expansion of some metals as determined by x-ray diffraction data. I. Platinum, tantalum, niobium and molybdenum *J. Appl. Phys.* **22** 424
[34] Imamura T, Shiota T and Hasuo S 1992 Fabrication of high quality Nb/AlO/sub x/-Al/Nb Josephson junctions. I. Sputtered Nb films for junction electrodes *IEEE Trans. Appl. Supercond.* **2** 1
[35] Todt C *et al* 2023 Development of Nb-gaas based superconductor-semiconductor hybrid platform by combining in situ DC magnetron sputtering and molecular beam epitaxy *Phys. Rev. Mater.* **7** 076201
[36] Wang C, Axline C, Gao Y Y, Brecht T, Chu Y, Frunzio L, Devoret M H and Schoelkopf R J 2015 Surface participation and dielectric loss in superconducting qubits *Appl. Phys. Lett.* **107** 162601
[37] Momma K and Izumi F 2008 *VESTA*: a three-dimensional visualization system for electronic and structural analysis *J. Appl. Crystallogr.* **41** 653
[38] Roberts B W 1976 Survey of superconductive materials and critical evaluation of selected properties *J. Phys. Chem. Ref. Data* **5** 581
[39] Dobrovolskiy O V and Huth M 2012 Crossover from dirty to clean superconducting limit in dc magnetron-sputtered thin Nb films *Thin Solid Films* **520** 5985
[40] Barends R, Vercruyssen N, Endo A, de Visser P J, Zijlstra T, Klapwijk T M, Diener P, Yates S J C and Baselmans J J A 2010 Minimal resonator loss for circuit quantum electrodynamics *Appl. Phys. Lett.* **97** 023508

[41] Zheng K, Kowsari D, Thobaben N J, Du X, Song X, Ran S, Henriksen E A, Wisbey D S and Murch K W 2022 Nitrogen plasma passivated niobium resonators for superconducting quantum circuits *Appl. Phys. Lett.* **120** 102601
[42] Calusine G *et al* 2018 Analysis and mitigation of interface losses in trenched superconducting coplanar waveguide resonators *Appl. Phys. Lett.* **112** 062601
[43] Gao R, Yu W, Deng H, Ku H-S, Li Z, Wang M, Miao X, Lin Y and Deng C 2022 Epitaxial titanium nitride microwave resonators: structural, chemical, electrical and microwave properties *Phys. Rev. Mater.* **6** 036202
[44] Geerlings K, Shankar S, Edwards E, Frunzio L, Schoelkopf R J and Devoret M H 2012 Improving the quality factor of microwave compact resonators by optimizing their geometrical parameters *Appl. Phys. Lett.* **100** 192601
[45] Wang H, Banerjee T, Farinha T G, Hanbicki A T, Fatemi V, Palmer B S and Richardson C J K 2024 Impact of etches on thin-film single-crystal niobium resonators (arXiv:2402.18051 [cond-mat.mtrl-sci])
[46] Murthy A A *et al* 2022 Developing a chemical and structural understanding of the surface oxide in a niobium superconducting qubit *ACS Nano* **16** 17257
[47] Halbritter J 2005 Transport in superconducting niobium films for radio frequency applications *J. Appl. Phys.* **97** 083904
[48] Kwon S *et al* 2018 Magnetic field dependent microwave losses in superconducting niobium microstrip resonators *J. Appl. Phys.* **124** 033903
[49] Liarte D B, Hall D, Koufalis P N, Miyazaki A, Senanian A, Liepe M and Sethna J P 2018 Vortex dynamics and losses due to pinning: dissipation from trapped magnetic flux in resonant superconducting radio-frequency cavities *Phys. Rev. Appl.* **10** 054057
[50] Wang C *et al* 2014 Measurement and control of quasiparticle dynamics in a superconducting qubit *Nat. Commun.* **5** 5836
[51] Nsanzineza I and Plourde B L T 2014 Trapping a single vortex and reducing quasiparticles in a superconducting resonator *Phys. Rev. Lett.* **113** 117002
[52] Song C, Heitmann T W, DeFeo M P, Yu K, McDermott R, Neeley M, Martinis J M and Plourde B L T 2009 Microwave response of vortices in superconducting thin films of Re and Al *Phys. Rev. B* **79** 174512
[53] Bothner D, Gaber T, Kemmler M, Koelle D and Kleiner R 2011 Improving the performance of superconducting microwave resonators in magnetic fields *Appl. Phys. Lett.* **98** 102504
[54] Nersisyan A *et al* 2019 *2019 IEEE Int. Electron Devices Meeting (IEDM)* (https://doi.org/10.1109/IEDM19573.2019.8993458)
[55] Woods W, Calusine G, Melville A, Sevi A, Golden E, Kim D, Rosenberg D, Yoder J and Oliver W 2019 Determining interface dielectric losses in superconducting coplanar-waveguide resonators *Phys. Rev. Appl.* **12** 014012
[56] Bal M *et al* 2024 Systematic improvements in transmon qubit coherence enabled by niobium surface encapsulation (arXiv:2304.13257 [quant-ph])
[57] Ganjam S *et al* 2023 Surpassing millisecond coherence times in on-chip superconducting quantum memories by optimizing materials, processes and circuit design (arXiv:2308.15539 [quant-ph])
[58] Dataset on Zenodo 2025 Data for 'the effect of niobium thin film structure on losses in superconducting circuits (available at: https://zenodo.org/records/15979909)
[59] Gubin A, Ilin K, Vitusevich S, Siegel M and Klein N 2005 Dependence of magnetic penetration depth on the thickness of superconducting nb thin films *Phys. Rev. B* **72** 064503
[60] Werthamer N R, Helfand E and Hohenberg P C 1966 Temperature and purity dependence of the superconducting critical field, H_{c2}. III. Electron spin and spin-orbit effects *Phys. Rev.* **147** 295
[61] Mayadas A F, Laibowitz R B and Cuomo J J 1972 Electrical characteristics of RF-sputtered single-crystal niobium films *J. Appl. Phys.* **43** 1287
[62] Pozar D 2011 *Microwave Engineering* 4th edn (Wiley) (available at: https://books.google.ch/books?id=JegbAAAAQBAJ)
[63] Probst S, Song F B, Bushev P A, Ustinov A V and Weides M 2015 Efficient and robust analysis of complex scattering data under noise in microwave resonators *Rev. Sci. Instrum.* **86** 024706
[64] Göppl M, Fragner A, Baur M, Bianchetti R, Filipp S, Fink J M, Leek P J, Puebla G, Steffen L and Wallraff A 2008 Coplanar waveguide resonators for circuit quantum electrodynamics *J. Appl. Phys.* **104** 113904
[65] Corveira Rodrigues I 2021 Coupling Harmonic oscillators to superconducting quantum interference cavities *PhD Thesis* Delft University of Technology (https://doi.org/10.4233/uuid:90c588b1-ebef-4ab8-b51f-b3221d8ad6cc)
[66] Phillips W A 1987 Two-level states in glasses *Rep. Prog. Phys.* **50** 1657
[67] w. Anderson P, Halperin B I and Varma C M 1972 Anomalous low-temperature thermal properties of glasses and spin glasses *Phil. Mag. A* **25** 1
[68] Gao J 2008 The physics of superconducting microwave resonators *PhD Thesis* California Institute of Technology (https://doi.org/10.7907/RAT0-VM75)
[69] Wang H *et al* 2009 Improving the coherence time of superconducting coplanar resonators *Appl. Phys. Lett.* **95** 233508
[70] Von Schickfus M and Hunklinger S 1977 Saturation of the dielectric absorption of vitreous silica at low temperatures *Phys. Lett. A* **64** 144
[71] Burnett J *et al* 2014 Evidence for interacting two-level systems from the 1/f noise of a superconducting resonator *Nat. Commun.* **5** 4119
[72] Sage J M, Bolkhovsky V, Oliver W D, Turek B and Welander P B 2011 Study of loss in superconducting coplanar waveguide resonators *J. Appl. Phys.* **109** 063915
[73] Haus H 1984 *Waves and Fields in Optoelectronics* (Prentice-Hall) (https://books.google.ch/books?id=AQUpAQAAMAAJ)
[74] Khalil M S, Stoutimore M J A, Wellstood F C and Osborn K D 2012 An analysis method for asymmetric resonator transmission applied to superconducting devices *J. Appl. Phys.* **111** 054510
[75] Github repository 2023 file 'S11fit.py' (available at: https://github.com/steelelab-delft/stlab/tree/master/misc/)
[76] Lifshitz R and Cross M C 2008 *Reviews of Nonlinear Dynamics and Complexity* (Wiley) (https://doi.org/10.1002/9783527626359.ch1)
[77] Bothner D, Rodrigues I C and Steele G A 2022 Four-wave-cooling to the single phonon level in Kerr optomechanics *Commun. Phys.* **5** 33
[78] Thomas C N, Withington S, Sun Z, Skyrme T and Goldie D J 2020 Nonlinear effects in superconducting thin film microwave resonators *New J. Phys.* **22** 073028
[79] de Visser P J, Goldie D J, Diener P, Withington S, Baselmans J J A and Klapwijk T M 2014 Evidence of a nonequilibrium distribution of quasiparticles in the microwave response of a superconducting aluminum resonator *Phys. Rev. Lett.* **112** 047004